Journal of Hazardous Materials 451 (2023) 131145

Contents lists available at ScienceDirect

Journal of Hazardous Materials

journal homepage: www.elsevier.com/locate/jhazmat

Research Paper

Insights into the weathering behavior of pyrite in alkaline soil through electrochemical characterizations: Actual hazards or potentially benefits?

Xiaonan Feng [a,b,1], Zhijie Chen [c,1], Shuai Wang [a,b], Ling Cen [a,b], Bing-Jie Ni [c], Qingyou Liu [a,*]

[a] Key Laboratory of High-temperature and High-pressure Study of the Earth's Interior, Institute of Geochemistry, Chinese Academy of Sciences, Guiyang 550081, China
[b] University of Chinese Academy of Sciences, Beijing 100039, China
[c] Centre for Technology in Water and Wastewater, School of Civil and Environmental Engineering, University of Technology Sydney, NSW 2007, Australia

HIGHLIGHTS

- Pyrite weathering generates γ-FeOOH and α-Fe_2O_3 with lesser environmental impacts.
- Pyrite weathering decreases the alkalinity of alkaline soils.
- Pyrite weathering prone to saline (91.87 g/m^2/y) than meadow (71.18 g/m^2/y) soil.
- Impure pyrite releases heavy ions pollute alkaline soil.
- T promotes weathering as v_{Meadow} = -3.37E5/T + 1.25E3, v_{Saline} = -2.73E5/T + 1.07E3.

GRAPHICAL ABSTRACT

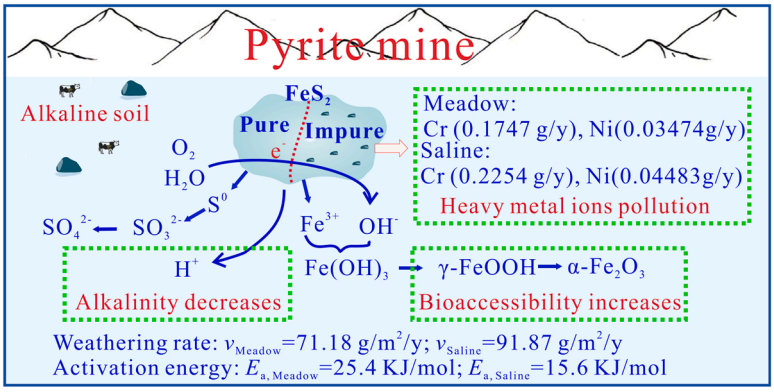

ARTICLE INFO

Editor: Haizhou Liu

Keywords:
Pyrite weathering
Alkaline soil
Electrochemical technique
Surface analysis
Environmental implications

ABSTRACT

Pyrite is the most common metal sulfide mineral in the crust and readily weathers under natural circumstances to release H^+ to acidify surrounding groundwater and soil, resulting in heavy metal ions in the surrounding environment (e.g., meadow and saline soils). Meadow and saline soils are two common, widely distributed alkaline soils and can affect pyrite weathering. Currently, the weathering behaviors of pyrite in saline and meadow soil solutions have not been systematically studied. Electrochemistry coupled with surface analysis methods were employed to study pyrite weathering behaviors in simulated saline and meadow soil solutions in this work. Experimental results suggest that saline soil and higher temperatures increase pyrite weathering rates due to the lower resistance and greater capacitance. Surface reactions and diffusion control the weathering kinetics, and the activation energies for the simulated meadow and saline soil solutions are 27.1 and 15.8 kJ mol^{-1}, respectively. In-depth investigations reveal that pyrite is initially oxidized to $Fe(OH)_3$ and S^0, and $Fe(OH)_3$ further transforms into goethite γ-FeOOH and hematite α-Fe_2O_3, while S^0 ultimately converts into sulfate. When these iron compounds enter alkaline soils, the alkalinity of soil changes, and iron (hydr)oxides effectively reduce the bioavailability of heavy metals and benefit alkaline soils. Meanwhile, weathering of natural pyrite ores

* Corresponding author.
E-mail address: liuqingyou@vip.gyig.ac.cn (Q. Liu).
[1] Xiaonan Feng and Zhijie Chen contribute equally to this work.

https://doi.org/10.1016/j.jhazmat.2023.131145
Received 9 October 2022; Received in revised form 7 February 2023; Accepted 2 March 2023
Available online 5 March 2023
0304-3894/© 2023 Elsevier B.V. All rights reserved.

containing toxic elements (such as Cr, As, and Cd) makes these elements bioavailable and potentially degrades the surrounding environment.

1. Introduction

Pyrite (FeS_2) is the most abundant and widespread metal sulfide on earth. Pyrite readily oxidizes in nature and causes acid mine drainage (AMD), heavy metal contamination and environmental pollution [31]. Currently, AMD and heavy metal contamination have attracted increasing attention. Li et al. [23] investigated the geochemical gradient characteristics of AMD from abandoned pyrite mines. Liu et al. [25] studied the source of heavy metal pollution in AMD by isotope analysis and principal component analysis technology and concluded that groundwater is significantly affected by soluble metals produced by pyrite oxidation. Naturally, pyrite oxidation is an electrochemical process [50], and thus, most previous studies focused on transformations of S and Fe to understand how pyrite behaved electrochemically. The consensus view of pyrite behavior [1,13] starts with pyrite oxidizing to elemental sulfur that ultimately transforms into sulfate. However, the intermediate sulfur species of pyrite oxidation are still controversial, with two prevailing viewpoints. One involves a polysulfide pathway and dissociation of S—S bonds to form an S^{2-} and S^0 passive film accompanied by further transformation to S_n^{2-} [37]. The other involves a thiosulfate pathway; elemental S oxidizes to a passive S^0 layer with the simultaneous release of $S_2O_3^{2-}$ into the solution, which rapidly converts to SO_3^{2-}, polythionates ($S_nO_6^{2-}$), and ultimately sulfate (SO_4^{2-}) [43,44].

Bare ground pyrite weathering under natural conditions causes an increase in heavy metal ions and acidity in the surrounding environment and leads to the potential deterioration of the surrounding environment. With the rapid development and utilization of metal sulfide minerals [7], pyrite weathering under natural conditions has attracted growing scientific interest. Rigby et al. [35] investigated the influences of bacteria and organic matter on pyrite weathered soil using kinetic experiments and confirmed that organic matter could mitigate the pyrite oxidation rate. Wang et al. [46] reported the weathering behavior of arsenopyrite under humic acid and concluded that higher temperature, concentration and acidity were more favorable for weathering. Caldeira et al. [5] pointed out that the composition of the solution affected the properties of the oxidation products of pyrite in alkaline solution, specifically, hematite was the main phase in the hydroxide medium and iron hydrate was the main phase in carbonate media. Meadow and saline soil are two common alkaline soils worldwide [49] that contain many inorganic substrates (e.g., Na^+, Cl^-, SO_4^{2-}, and HCO_3^-). The content of pyrite in alkaline soils increases significantly with increasing mining activities [17,42], and in return, the Cl^- and HCO_3^- of alkaline soils affect the pyrite weathering behavior. To date, the weathering behaviors of pyrite in alkaline soil have not been reported regarding pyrite weathering thermodynamics, kinetics, and reaction mechanisms.

In this study, different electrochemical measurements combined with different surface analysis techniques were used to investigate the weathering behavior of pyrite in simulated meadow and saline soils, with the following purposes: (1) reveal transformations of Fe and S from pyrite weathering, (2) quantitatively identify the pyrite weathering rate, and (3) ultimately determine whether pyrite is hazardous or helpful in alkaline soil remediation.

2. Materials and methods

2.1. Preparation of pyrite samples, meadow, and saline soil solutions

Pyrite samples, including single crystal and impure pyrite, were obtained from the Xingwen pyrite mine, Sichuan Province, China. X-ray diffraction (Empyrean, Panaco of Netherlands) confirms that the single crystal samples are pyrite, and electron microprobe (JXA-8230, JEOL) results show that pyrite contains Fe (46.89, wt%) and S (52.96, wt%). Levels of trace metal elements in the impure pyrite samples are listed in Table S1.

The pyrite single-crystal specimens were cut into rectangles (0.5 cm (a) × 0.5 cm (b) × 1.0 cm (h)), the upper surface was attached to a copper conductor using silver paint, and the other parts were sealed with epoxy resin. The epoxy resin of the underside was ground to expose the pyrite electrode surface. Other pyrite specimens were crushed, selected, ground, and ultimately yielded 80 μm pure pyrite powders.

The simulated meadow soil and saline soil solutions were prepared according to the physicochemical properties of meadow soil and saline soil (GB50021-2008; [24]). Their chemical compositions are listed in Table S2; H_2SO_4 and NaOH solutions were used to adjust the pH levels to 7.4 and 8.6, respectively. All electrolytes were prepared using ultrapure water and analytical-grade chemicals. Temperature is one of the important factors that affect pyrite weathering. In this work, five typical ambient temperatures of 5 °C, 15 °C, 25 °C, 35 °C and 45 °C related to different longitudes, latitudes, and seasons were selected as experimental temperatures.

2.2. Batch immersion experiments

During the block pyrite batch immersion experiments, twenty polyethylene bottles were filled with the simulated solutions. Ten polyethylene bottles contained 60 mL of simulated meadow soil, and the other ten contained 60 mL of simulated saline soil solution. A polished block pyrite sample (0.5 cm × 0.5 cm × 0.05 cm) was immersed in each solution. After weathering for 3 and 10 weeks, they were analyzed by scanning electron microscopy (SEM) and energy-dispersive X-ray spectroscopy (EDS).

The powder immersion experiments involved adding 0.5 g of pyrite powder samples into each solution. After the powder samples were weathered for 10 weeks, they were analyzed by Fourier transform infrared spectroscopy (FTIR) and X-ray photoelectron spectroscopy (XPS). Avantage 5.948 and XPSPEAK41 software were used to fit and analyze the related chemical state distributions and elemental content (at%) data corrected by the C1 s peak at 284.8 eV. S 2p spectra were fitted by doublets with the same full width at half maximum and intensity ratios of 2:1 and spin-orbit splitting of 1.18 eV, and Fe 2p spectra were fitted by the theoretical core p level multiplet structures for free transition metal ions (GS multiplets).

The pH levels for all solutions were continuously monitored until the immersion experiments concluded. All bottles were sealed with a semipermeable membrane to maintain free airflow and reduce water evaporation. A digital thermostatic water bath maintained temperatures at 5 ± 0.1, 15 ± 0.1, 25 ± 0.1, 35 ± 0.1, and 45 ± 0.1 °C. All soaking experiments were performed in duplicate.

2.3. Electrochemical experiments

A PARSTAT 2273 electrochemical workstation coupled to a three-electrode system was used to perform all electrochemical experiments. A platinum electrode and a saturated calomel electrode (SCE) acted as the counter electrode and reference electrode, respectively, and the pyrite electrode was used as the working electrode. All potentials are reported relative to the SCE (0.245 V vs. standard hydrogen electrode at 25 °C). All electrochemical tests were initiated only after the open circuit potential (OCP) achieved a quasi-steady state (< 1.0 mV per 150 s). The cyclic voltammetry (CV) potential sweep from − 1.2 to 0.6 V at a rate of 5.0 mV s^{-1}. Polarization measurements were carried out at a sweep rate of 10.0 mV S^{-1} from − 0.25 V to + 0.25 V (vs. OCP). Electrochemical

impedance spectroscopy (EIS) tests were conducted at the OCP in a frequency range from 10^{-3} to 10^{5} Hz with an amplitude of 10.0 mV. Polarization and impedance data were fitted by PowerSuit and ZSimpWin software, respectively. At least three parallel experiments ensured repeatability, and the error was less than 3 %.

2.4. Physicochemical characterizations

Pristine and eroded pyrite samples were used for characterization analysis. SEM images were obtained using a JSM-6460LV equipped with EDS and used to observe and identify surface morphology changes, including elemental composition analysis. Raman spectra were collected on a British Renishaw (Reflex type microscopic confocal laser Raman spectrometer) instrument with the following instrument parameters: < 30 s laser time, 514 nm wavelength, 50 mW (5 %) power to avoid laser damage to the sample surface. FTIR measurements were performed from 400 to 4000 cm^{-1} (Bruker Vertex 70). XPS data were obtained on an ESCALAB 250XI X-ray photoelectron spectrometer coupled with a monochromatic Al-Ka X-ray (1486.6 eV).

3. Results and discussion

3.1. Effect of temperature on pyrite weathering

The environmental conditions (e.g., temperature) of soils profoundly influence the pyrite weathering process. The OCP value reflects the thermodynamic properties of the system, and a more negative OCP signifies that pyrite erodes more readily. How the OCP varied with time for pyrite electrodes in meadow and saline soil solutions at different temperatures is shown in Fig. 1(a, c). In both solutions, pyrite reaches a quasi-steady state after ~ 30 min, suggesting that the pyrite surface has spontaneously formed a passive film [1]. Regardless of meadow or saline soil solutions, OCP values become more negative at higher temperatures, which indicates that pyrite is weathered more readily at high temperatures. OCP values in saline soil solution were always more positive than those in meadow soil solutions at the same temperature; thus, pyrite eroded more readily in meadow soil than in saline soil (Table 1).

Pyrite weathering releases metal ions and increases environmental acidity. The weathering rate is a key parameter to evaluate the environmental impact of pyrite weathering on soil over time, and temperature is the most important external influence factor. Polarization curves provide information on the electrolytic process and how various factors affect the electrode [27], with a particular emphasis on the rates of ions leaving the material surface [38]. These curves were used to obtain pyrite weathering rates.

The similar *E-i* profiles of pyrite samples suggest that pyrite weathers in the same way (Fig. 1(b, d)). Moreover, the curves shift dramatically to the lower right as the temperature increases, implying that higher temperatures induce a greater corrosion current density and a more negative corrosion potential. The corrosion current density (i_{corr}) and corrosion potential (E_{corr}) were known from polarization curves based on the Tafel extrapolation theory [3]. The weathering rate of pyrite can be obtained via the Faraday equation [12].

$$v = \frac{Mi_{corr}}{nF} \tag{1}$$

Where v (g m^{-2} y^{-1}) is the weathering rate, i_{corr} (μA cm^{-1}) represents the corrosion current density, M (g mol^{-1}) is the molecular mass, n (dimensionless) is the metal valence, and F (C mol^{-1}) is the Faraday constant.

Table 2 lists the weathering rates (v) of pyrite in the simulated meadow and saline soil solutions. The polarization curve results show a

Table 1
OCP of pyrite in the simulated meadow and saline soil solutions at different temperatures.

	Temperature (°C)	5	15	25	35	45
OCP(mV)	Meadow	70.6	44.3	20.4	5.47	-27.1
	Meadow	76.9	59.6	45.9	22.7	-21.3

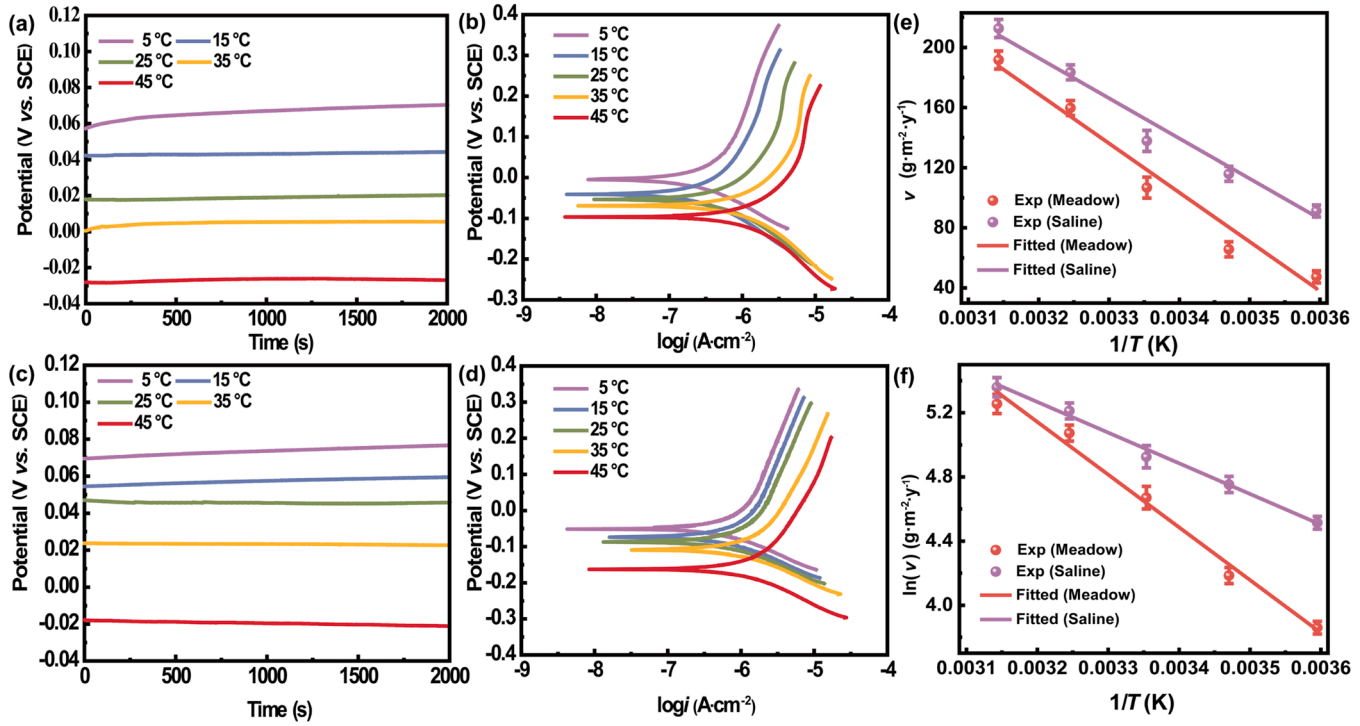

Fig. 1. OCP study (a) and Polarization curves study (b) in simulated meadow soil solutions at different temperatures; OCP study (c) and Polarization curves study (d) in simulated saline soil solutions at different temperatures; Variations in the weathering rate (e) and ln(v) (f) with 1/T.

Table 2
Electrochemical parameters of pyrite electrodes in meadow and saline solutions at different temperatures.

Alkaline soil	T (°C)	E_{corr} (mV)	i_{corr} (μA cm^{-2})	v (g m^{-2} y^{-1})
Meadow	5	-4.40	0.520	47.46
	15	-45.2	0.720	65.71
	25	-52.2	1.17	106.77
	35	-68.9	1.75	159.71
	45	-111	2.10	191.65
Saline	5	-50.7	1.00	91.26
	15	-73.5	1.27	115.90
	25	-82.5	1.51	137.80
	35	-108	2.01	183.43
	45	-163	2.33	212.64

E_{corr}: corrosion potential; i_{corr}: corrosion current density; v: weathering rate.

linear relationship between the weathering rate (v) and the temperature ($1/T$) (Fig. 1c): v_{Meadow} = -3.37E5/T + 1.25E3 (R^2 = 0.9751) and v_{Saline} = -2.73E5/T + 1.07E3 (R^2 = 0.9707), respectively. These results confirm that higher temperatures accelerate pyrite weathering and that pyrite weathered faster in saline soil regardless of the soil solution. Using 25 °C as an example, the v_{Meadow} of pyrite was 71.18 g m^{-2} y^{-1}, meaning 71.18 g Fe(III) was released yearly when the FeS_2 area was 1 m^2 at 25 °C. In contrast, saline soil releases 91.87 g of Fe(III).

EIS was further used to explain the different weathering rates, as it can reveal the electrochemical kinetics of processes, resistances, and capacitances of electrochemical reactions [22]. Fig. 2 shows Nyquist and Bode plots of pyrite in the simulated meadow and saline soil solutions. Both Nyquist plots (Fig. 2(a, d)) consist of two capacitive loops that correspond to the Bode plots (Fig. 2(b, e)) of two time constants. The first (high frequency) capacitive loop corresponds to the passive film resistance R_f and can be ascribed to pseudo-capacitance impedance coupling. The second (low frequency) involves the charge transfer resistance R_t and represents the resistance between the electrode and outer Helmholtz layer [47]. Fig. S1 shows the equivalent electrochemical circuit, which simulates the pyrite/electrolyte interface. R_s represents the solution resistance, while CPE_f and CPE_{dl} are constant phase elements replacing the passive film capacitance and the charge transfer capacitance at the double layer, respectively. For both solutions, as the temperature increases, pyrite exhibits smaller R_f and R_t values but larger CPE_f and CPE_{dl} levels (Table 3). These results reveal that higher temperatures accelerated pyrite weathering in alkaline soil by dramatically decreasing the charge migration resistance between the double layer and the passivation film. Furthermore, when comparing pyrite R_f and R_t values, R_t for either meadow or saline soil solutions is similar at the same temperature; however, the R_f in saline soil is much smaller than that in the meadow solution and suggests that smaller passivation resistance is the primary factor responsible for the faster pyrite erosion in the saline soil.

3.2. Pyrite weathering activation energy

Activation energy is the minimum amount of energy required to convert a normal stable molecule into a reactive molecule. According to the Arrhenius equation, the activation energy (E_a) is expressed as:

$$\ln v = -\frac{E_a}{RT} + \ln A \quad (2)$$

where v (mol L^{-1} s^{-1}) represents the reaction rate constant, A (mol L^{-1} s^{-1}) is the pre-exponential factor, R (J mol^{-1} K^{-1}) is the molar gas constant, e (dimensionless) represents the Napierian base, T (K) denotes the absolute temperature and E_a (J mol^{-1}) is the activation energy.

Fig. 1f shows a linear relationship between ln$v$ and $1/T$: $\ln v_{Meadow}$ = -3263.85/T + 15.581 (R^2 = 0.9871) and $\ln v_{Saline}$ = -1903.7/T + 11.352 (R^2 = 0.993). The activation energies of pyrite weathering in the simulated meadow and saline soil solutions are 27.1 and 15.8 kJ mol^{-1}, respectively. Both E_a values are < 40 kJ mol^{-1}, indicating that pyrite weathering readily occurs in alkaline soils [2]. Laidler [19] noted that lower activation energies corresponded to faster

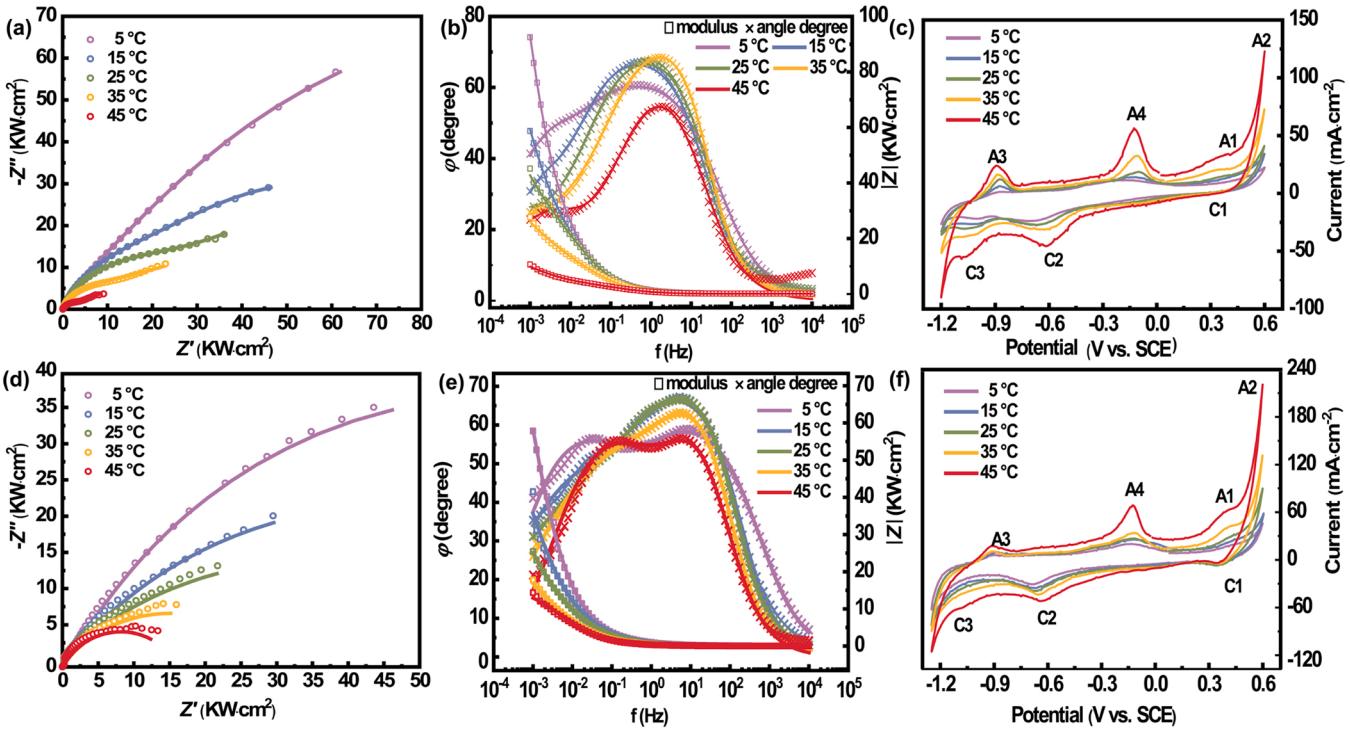

Fig. 2. Nyquist plots (a), Bode plots (b) and CV curves (c) for pyrite in simulated meadow soil solutions at different temperatures; Nyquist plots (d) and Bode plots (e) and CV curves (f) for pyrite in simulated saline soil solutions at different temperatures, where ○, □ and × represent the experimental values and – represents the simulated values.

Table 3
Equivalent circuit model parameters for pyrite in meadow and saline solutions at different temperatures.

Soil	T (°C)	CPE_f, Y_0 (S cm^{-2} s^{-n})	n	R_f (Ω cm^2)	CPE_{dl}, Y_0 (S cm^{-2} s^{-n})	n	R_t (Ω cm^2)	χ^2
Meadow	5	2.10E-4	0.709	6.38E4	2.03E-4	0.742	1.65E5	1.42E-4
	15	2.50E-4	0.790	3.72E4	7.40E-4	0.757	6.65E4	1.40E-3
	35	2.63E-4	0.765	5.62E3	1.21E-3	0.443	4.60E4	2.37E-3
	45	3.17E-4	0.766	3.61E3	1.67E-3	0.568	1.52E4	3.19E-3
Saline	5	2.60E-4	0.700	4.81E3	1.58E-4	0.690	1.18E5	6.34E-4
	15	2.89E-4	0.801	3.42E3	2.44E-4	0.520	9.09E4	1.34E-3
	25	3.07E-4	0.829	1.30E3	2.57E-4	0.444	7.52E4	3.04E-4
	35	3.63E-4	0.835	5.80E2	4.32E-4	0.524	3.07E4	3.88E-4
	45	4.24E-3	0.800	4.87E2	5.24E-4	0.640	1.59E4	1.25E-3

R_f: passive film resistance; R_t: charge transfer resistance; n: dimensionless number.
CPE_{dl}: constant phase element of double layer; CPE_f: constant phase element of passive film.

reaction rates. A previous study [21] showed that an E_a over 20 kJ mol^{-1} meant the reaction was controlled by the surface, while an E_a less than 20 kJ mol^{-1} indicated a diffusion control process. Hence, the obtained E_a of pyrite weathering in meadow soil is 27.1 kJ mol^{-1}, which suggests that pyrite weathering in meadow soil is controlled by surface reactions, whereas for pyrite weathering in saline soil, E_a (15.8 kJ mol^{-1}) < 20 kJ mol^{-1}, suggesting that pyrite weathering was diffusion controlled. These results are in accordance with previous EIS results, that is, a very small R_f in saline soil benefits ion diffusion. In contrast, the large R_f for the simulated meadow soil promotes a charge aggregate on the pyrite surface.

3.3. Cyclic voltammetry study

Cyclic voltammetry (CV) provides information about the redox reaction taking place at the electrode interface. In this work, CV was used to study the specific weathering process of pyrite under various soil conditions. CV curves of pyrite electrodes in the simulated meadow and saline soil solutions at various temperatures are presented in Fig. 2(c, f). All curves show similar *E-I* profiles, indicating the same electrochemical interaction mechanism. Higher temperatures cause a larger corrosion current at the same sweep potential, and thus, higher temperatures accelerate pyrite weathering. There are four anodic and three cathodic peaks on these curves. During the positive scan, the first anode peak (A1) appeared at approximately 0.4 V, likely caused by the oxidation of pyrite to form ferric hydroxides with elemental sulfur, as shown in Reaction (3) [1,13]. The second anodic peak (A2) appears at ~ 0.6 V, corresponding to further oxidization of pyrite to ferric hydroxides and sulfates at higher potentials, as shown in Reaction (4) [1,40]. During the negative scan, the first cathodic peak (C1) appears at approximately 0.3 V due to iron hydroxide reduction [15], the second (C2) is located at − 0.6 V due to the reduction of elemental sulfur [13], and the third (C3) appears at approximately − 1.1 V owing to the reduction of pyrite itself. FeS exists as a stable precipitate in neutral or alkaline solutions [40]. During the positive return sweep, the third anodic peak (A3) observed at − 1.0 V is ascribed to the oxidation of elemental iron [13]. The last anodic peak, A4 ~ − 0.1 V is due to the oxidation of HS^- [1]. The pertinent reactions are shown below.

$$A1:\ FeS_2 + 3H_2O \rightarrow Fe(OH)_3 + 2S + 3H^+ + 3e^- \quad (3)$$

$$A2:\ FeS_2 + 11H_2O \rightarrow Fe(OH)_3 + 2SO_4^{2-} + 19H^+ + 15e^- \quad (4)$$

$$C1:\ Fe(OH)_3 + e^- \rightarrow Fe(OH)_2 + OH^- \quad (5)$$

$$C2:\ S^0 + 2e^- + H_2O \rightarrow HS^- + OH^- \quad (6)$$

$$C3:\ FeS_2 + 2e^- + H_2O \rightarrow FeS + HS^- + OH^- \quad (7)$$

$$FeS_2 + 4e^- + 2H_2O \rightarrow Fe + 2HS^- + 2OH^- \quad (8)$$

$$A3:\ Fe + 2OH^- \rightarrow Fe(OH)_2 + 2e^- \quad (9)$$

$$Fe + OH^- + HS^- \rightarrow FeS + H_2O + 2e^- \quad (10)$$

$$A4:\ HS^- \rightarrow H+ + S^0 + 2e^- \quad (11)$$

3.4. Pyrite surface morphology analysis

The variation in the morphology of pyrite during weathering was then investigated with SEM measurements. The pristine pyrite is smooth, clean, and homogeneous (Fig. S2). After being weathered for 3 weeks, all the pyrite surfaces (Fig. 3) appear rough and inhomogeneous, which is accompanied by corrosion pitting and prominent drusy areas, especially noticeable in some cracks on the surface. Higher temperatures increase the number and size of the micro-particles on the pyrite surface. After weathering for 10 weeks, all pyrite specimens (Fig. S3) show significant erosion and are covered with a thick flocculent film and deep honeycomb holes instead of perfect crystalline features. Using pyrite weathered in saline soil solution as an example, the corrosion film on the pyrite surface is almost crystalline at 5 °C, then changes to a flocculent film at 15 °C, and gradually grows larger as the temperature increases to 45 °C.

Table S3 shows the elemental composition of the pristine and weathered pyrite specimens. The results reveal that pristine pyrite contains Fe (31.8 at%) and S (68.2, at%), agreeing with the molar ratios of Fe and S in pyrite. Eroded pyrite specimen analyses indicate that the surface precipitates consist of O, S, and Fe, and higher temperatures result in higher levels of atomic oxygen and lower levels of atomic sulfur. Notably, Fe levels (at%) decrease at lower temperatures (from 5 to 25 °C) and increase at higher temperatures (from 25 to 45 °C). This is due to the prominent formation of iron polysulfides and relatively few iron oxides at low temperatures. However, higher temperatures favor iron oxides, and polysulfides are less stable, which is further confirmed by Raman and XPS analyses. Furthermore, pyrites weathered in the saline soil solution always contain more oxygen and less sulfur at the same temperature than those in the meadow soil solution, which suggests that pyrite suffers more significant erosion in saline soil than in the meadow soil solution. All results are in line with the electrochemical data.

3.5. Mineralogical phase analysis

Raman spectra of initial pyrite samples and weathered samples are presented in Fig. 4(a, c). The peaks appearing at 338 and 372 cm^{-1} are the characteristic pyrite Raman peaks in the initial pyrite sample [20,41]. After weathering in meadow soil solutions, three new peaks appear at ~ 220, 280, and 596 cm^{-1}. The peak at ~ 220 cm^{-1} can be ascribed to sulfur (S^0), and the other two peaks belong to goethite (γ-FeOOH) [6,10,48]. Pyrite weathered in saline soil solutions at 5, 15 and 25 °C affords Raman spectra identical to those weathered in the meadow soil. However, at 35 or 45 °C, two additional peaks appear: one at 443–475 cm^{-1} is assigned to polysulfide (S_n^{2-}) [32], and the other at

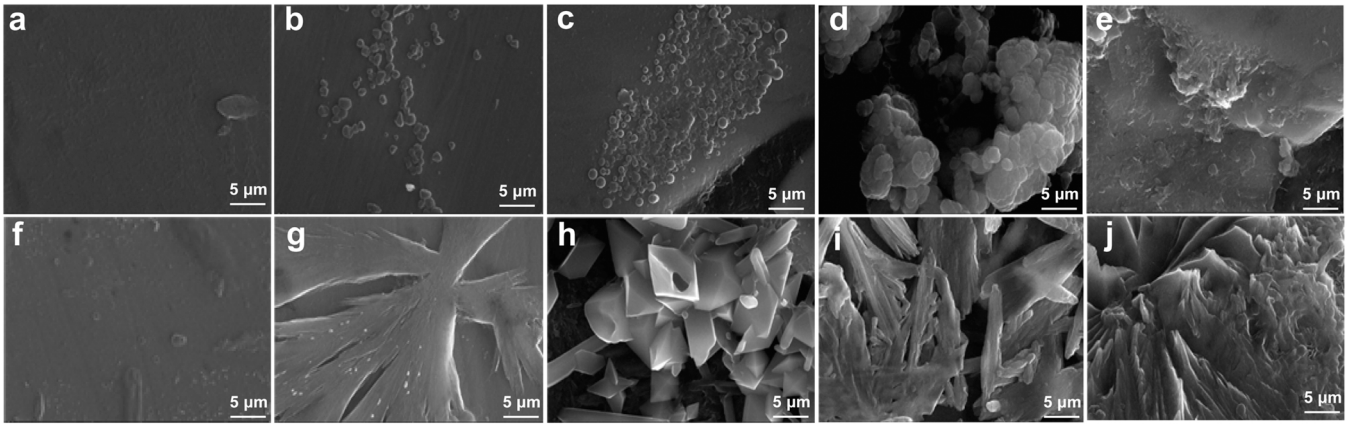

Fig. 3. SEM images of the pyrite after weathered for 3 weeks. (a) 5 °C, (b) 15 °C, (c) 25 °C, (d) 35 °C, (e) 45 °C in simulated meadow soil solutions; (f) 5 °C, (g) 15 °C, (h) 25 °C, (i) 35 °C, (j) 45 °C in simulated saline soil solutions.

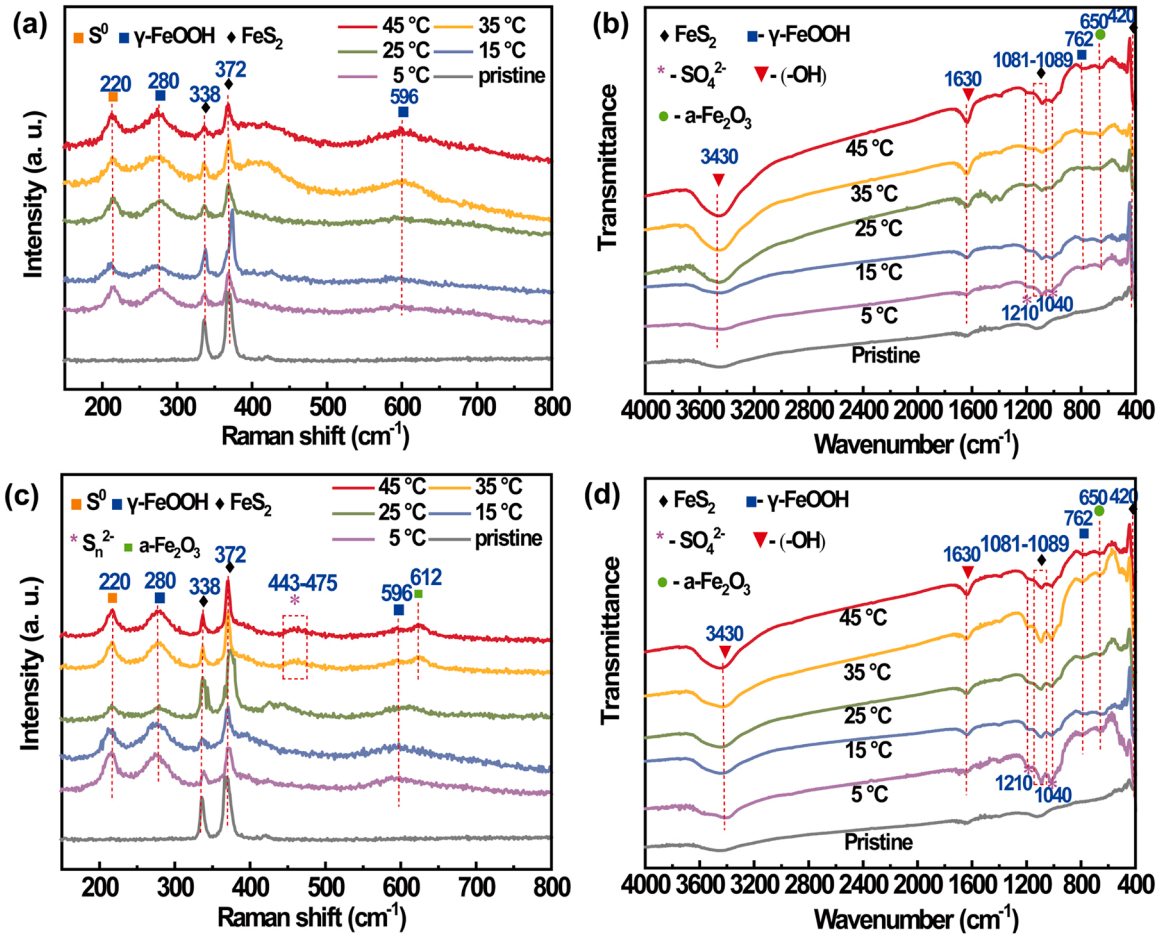

Fig. 4. Raman (a) and FTIR (b) spectra of the pristine and weathered pyrite in simulated meadow soil solutions; Raman (c) and FTIR (d) spectra of the pristine and weathered pyrite in simulated saline soil solutions.

612 cm^{-1} is attributed to hematite (α-Fe_2O_3) [20,39]. Table S4 summarizes the Raman peak positions for FeS_2, S^0, S_n^{2-}, γ-FeOOH, and α-Fe_2O_3.

Fig. 4(b, d) shows the FTIR spectra of the pristine and weathered pyrite specimens. For pristine pyrite, absorption bands at 420 cm^{-1} and 1081–1089 cm^{-1} are attributed to Fe–S and S–S stretching vibrations in the pyrite lattice [45]. The bands at 3430 and 1630 cm^{-1} are due to O-H stretching vibrations associated with adsorbed water molecules [5]. All weathered pyrite samples result in identical FTIR spectra. The multiple bands observed between 1040 and 1210 cm^{-1} are ascribed to the asymmetric sulfate S-O stretch, which normally splits into doubly or triply degenerate peaks from 1040 to 1210 cm^{-1} [11]. The peak at 762 cm^{-1} corresponds to goethite (γ-FeOOH) [9], and the peak at 650 cm^{-1} corresponds to hematite (α-Fe_2O_3) [5]. Table S5 summarizes the FTIR spectra from this work and previous studies.

3.6. Surface elemental composition analysis

Fig. 5 and Table S6 display the Fe *2p* and S *2p* spectra and binding energy states for pristine and weathered pyrite. For the Fe $2p_{(3/2)}$ of pristine pyrite, one obvious peak is observed at a binding energy (BE) of 707.0 eV, which agrees with ferrous ions from lattice pyrite [28], and a minor peak at 708.5 eV is due to iron from ferric monosulfide [43,44]. After weathering, additional peaks are observed at 708.8, 709.4, 710.6, 711.8, and 713.4 eV, which can be attributed to Fe(II)O or Fe(III)O formed by pyrite oxidation. Specifically, peaks at 708.8 and 709.4 eV correspond to Fe(II)O [43,44]. The peak at 710.6 eV is assigned to hematite (α-Fe_2O_3) [8], while peaks at 711.8 and 713.4 eV are assigned to goethite (γ-FeOOH) and ferric hydroxide ($Fe(OH)_3$) [4] and are likely due to iron hydroxide instability and its subsequent conversion into relatively stable ferric oxides. Ferrous ion levels decrease as the temperature increases, which indicates that more ferrous ions are converted to ferric ions. These results agree well with electrochemical tests, Raman, and FTIR measurements.

For the S *2p* spectra of both pristine and weathered pyrite, five pairs of characteristic double peaks appear at BEs of 161.8, 162.7, 163.6, 165, and 168.9 eV, which can be indexed to mono-sulfide (S^{2-}) [30], disulfide (S_2^{2-}) [30], sulfur (S^0) or polysulfide (S_n^{2-}) [20], sulfite (SO_3^{2-}) [4] and sulfate (SO_4^{2-}) [8], respectively.

For pristine pyrite, the major doublet at 162.7 eV is assigned to disulfide from pyrite itself. The peak at 161.8 eV is ascribed to FeS formed by the fracture of S—S bonds, as shown in reaction (12) [29], and is likely due to weaker S—S bonds relative to Fe—S bonds, which makes S^- ions more susceptible to disproportionation reactions, as shown in reaction (13) [26]. Subsequently, S^{2-} readily oxidizes to sulfate due to its instability [37]. The additional peak at 163.6 eV is likely due to S^0 or S_n^{2-}, and it is difficult to distinguish and separate due to their overlapping binding energy positions [28]. Combined with the above Raman results, we conclude that the oxidation products of FeS_2 contain both elemental sulfur and polysulfide produced via reaction (14) [26]. The slight peak at 165 eV is thought to be SO_3^{2-}, which exists as an intermediate product but in extremely low concentration. The peak at 168.9 eV is attributed to SO_4^{2-}, which is the final and most thermodynamically stable oxidation product and is confirmed by the accumulation of SO_4^{2-} on the surface as the temperature increases.

$$\text{Fe-S-S} \rightarrow \text{Fe(III)-S} + S^- \quad (12)$$

$$2S^- \rightarrow S^0 + S^{2-} \quad (13)$$

$$S^{2-} + S^0_{n-1} \rightarrow S^{2-}_n \quad (14)$$

3.7. Summary of the pyrite weathering mechanism

Based on the results obtained and discussed above, Fig. 6 presents the pyrite weathering mechanism. The element Fe of FeS_2 is first oxidized to hydroxides (reaction (3)), then transforms to goethite (γ-FeOOH) via reaction (15) [34] and is terminally oxidized to hematite (α-Fe_2O_3). Many researchers believe the process is shown as reactions (16) and (17) [18]. In this study, the Raman peaks at 280 and 596 cm^{-1} are ascribed to goethite (γ-FeOOH), and the peak at 612 cm^{-1} is attributed to hematite

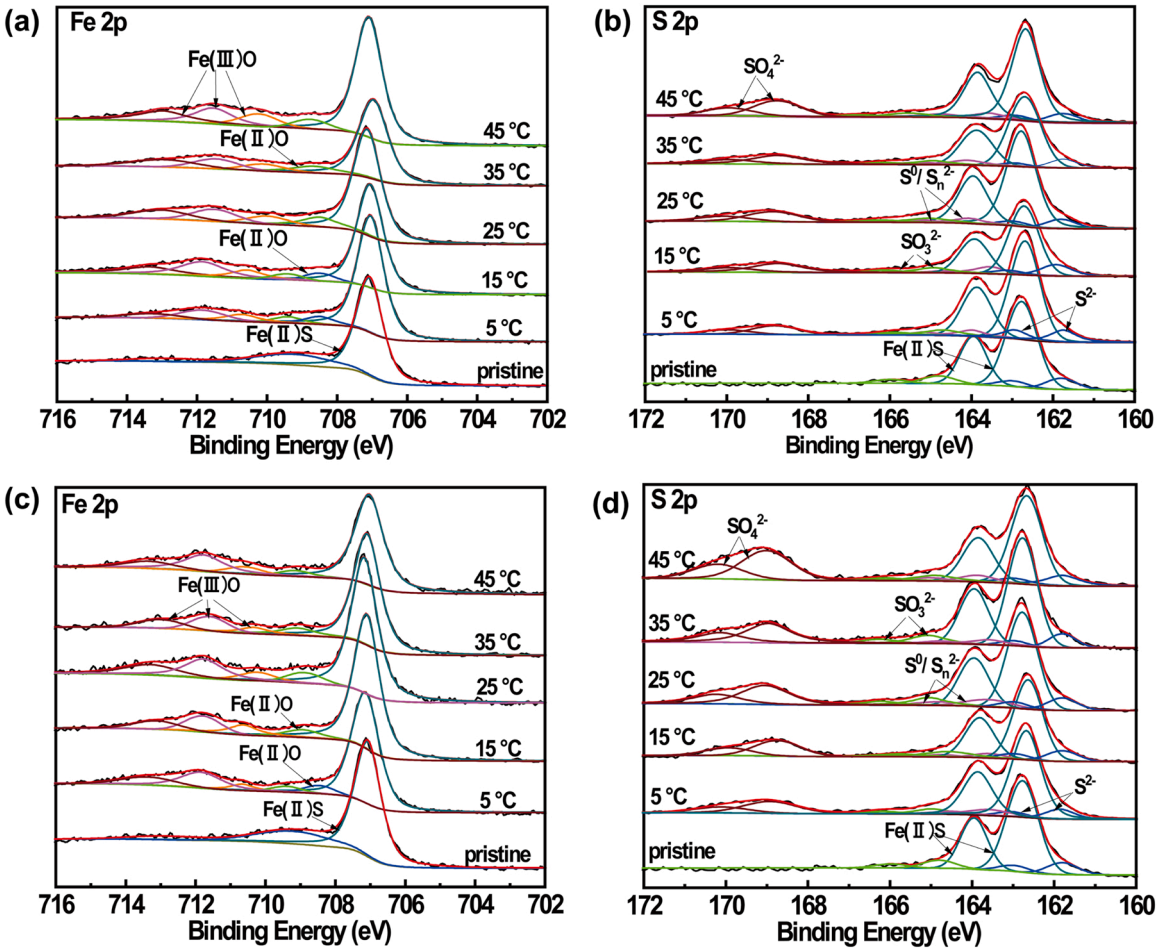

Fig. 5. XPS spectrum of the pristine and weathered pyrite at different temperatures. (a) Fe 2p spectrum in simulated meadow soil solutions; (b) S 2p spectrum in simulated meadow soil solutions; (c) Fe 2p spectrum in simulated saline soil solutions; (d) S 2p spectrum in simulated saline soil solutions.

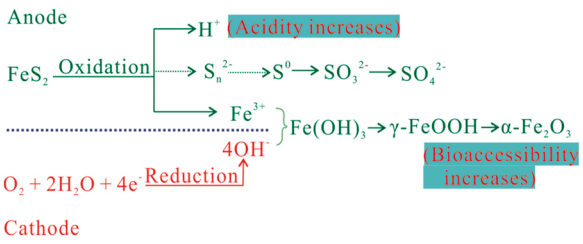

Fig. 6. The weathering mechanism of pyrite in simulated alkaline soil solutions.

(α-Fe_2O_3). The peak at 762 cm^{-1} corresponds to goethite (γ-FeOOH) [9], and the peak at 650 cm^{-1} corresponds to hematite (α-Fe_2O_3) [5] in the FTIR spectra. In XPS analysis, the observed peaks at 708.8, 709.4, 710.6, 711.8, and 713.4 eV are attributed to Fe(II)O or Fe(III)O formed by pyrite oxidation.

$$Fe(OH)_3 + 3H^+ \rightarrow \gamma\text{-}FeOOH + 3H_2O \quad (15)$$

$$8\gamma\text{-}FeOOH \rightarrow 4\gamma\text{-}Fe_2O_3 + 4H_2O \rightarrow 4\alpha\text{-}Fe_2O_3 + 4H_2O \quad (16)$$

$$2\gamma\text{-}FeOOH \rightarrow 2\alpha\text{-}FeOOH \rightarrow \alpha\text{-}Fe_2O_3 + H_2O \quad (17)$$

Meanwhile, the element S of FeS_2 is oxidized to the S^0 passivation film (reaction (2)). During the oxidized progress of element S, the reaction products polysulfide (S_n^{2-}) occur via reactions (12)–(14), and the S^0 passive film ultimately transforms to stable sulfate (SO_4^{2-}) as reaction (18) [30]. In this work, S^0 can be observed from the Raman and XPS data, S_n^{2-} can be observed from the Raman spectra, SO_3^{2-} can be observed from XPS data, and SO_3^{2-} can be observed from FTIR and XPS spectra. Thus, we think that the intermediate sulfur conversion pathway includes both the thiosulfate pathway [43,44] and the polysulfide pathway [37].

$$2S^0 + 3O_2 + 2H_2O \rightarrow 2SO_4^{2-} + 4H^+ \quad (18)$$

Furthermore, H^+ ions also released out with the element Fe and S oxidized from reactions (3), (4), and (11). Above all, higher temperature only accelerated the oxidative dissolution without changing the interaction mechanism. Furthermore, H^+ ions are also released with the elements Fe and S oxidized from reactions (3), (4), and (11). Above all, higher temperature only accelerated oxidative dissolution without changing the interaction mechanism.

4. Environmental implications

4.1. Pyrite weathering affects surroundings pH

One well-known environmental problem associated with pyrite weathering is acid drainage pollution. Fig. 7 shows how pH varied with time as 0.5 g pyrite weathered in 60 mL simulated soil solutions. Both pH values decrease dramatically during initial pyrite weathering (20 min), and the pH levels for both simulated solutions gradually decrease and stabilize after approximately 50 days. A large amount of pyrite was used to better reflect the release of hydrogen ions from pyrite in alkaline solutions and resulted in a relatively short interval for the solution to change from alkaline to acidic. These results reveal that pyrite weathering in alkaline soil releases H^+ to acidify surrounding circumstances, such as groundwater and soil, which may neutralize the soil or turn it acidic if pyrite levels are sufficient. Higher temperatures promote the pH shift in alkaline soil toward increased acidity and might open an avenue for alkaline soil remediation.

4.2. Pure vs. impure pyrite weathering: potential remediation or heavy metal ions pollution?

Weathering of pure pyrite involves transformations into iron hydroxides $Fe(OH)_3$, goethite γ-FeOOH, and hematite α-Fe_2O_3. Goethite and hematite have stronger biological activities due to their reactive surface functional groups and high specific surface area [14]. They offer the potential for effective remediation of heavy metal-contaminated soils by reducing the bioavailability of heavy metals in soil and water that result from partial dissolution and adsorption/precipitation reactions between amendments and metal(loid)s [16]. Moreover, these modifications have positive effects on bacterial diversity in soil, and many researchers have shown that soil function improves as bacterial diversity increases [33]. Iron oxide particles also play an important role in biomedical applications due to their semiconductor characteristics, magnetic properties, and lack of toxicity [36].

Using pyrite ores from the Xingwen mine (a famous “pyrite mine” of Sichuan province, China) as an example of impure pyrite (Table S1), weathering transforms pyrite into iron hydroxides and iron oxide particles with a concomitant release of heavy metal ions into the alkaline soils. Polarization results indicated Fe(III) release rates of 71.18 and 91.87 g m^{-2} y^{-1} for simulated meadow and saline soil solutions at 25 °C. Additionally, chromium and nickel, two common heavy metals found in Xingwen Mine pyrite ores, are also released (0.1747 and 0.2254 g of Cr; 0.03474 and 0.04483 g of Ni from meadow and saline soils, respectively), which indicates that impurities released from pyrite ore weathering pose potential pollution problems.

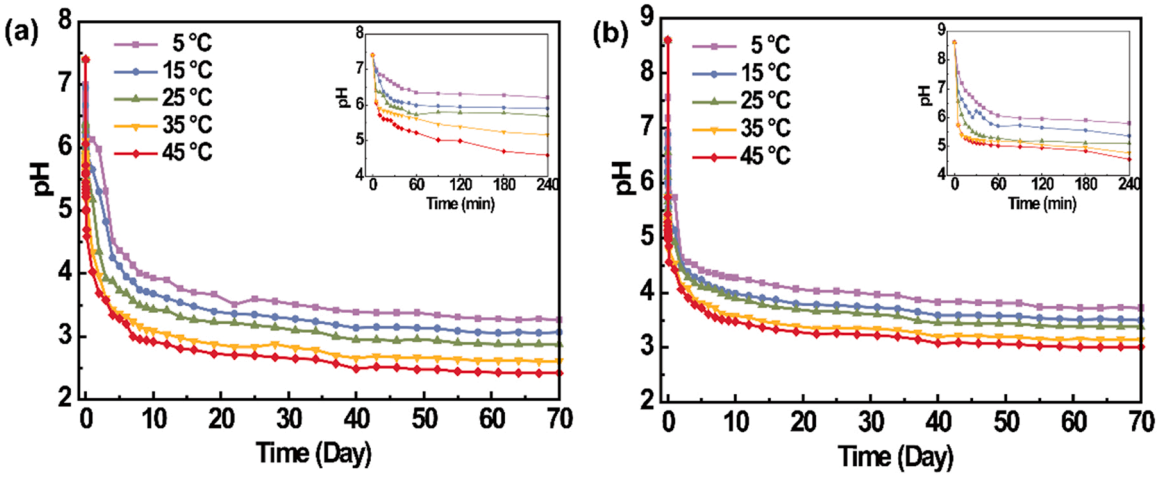

Fig. 7. The pH variation of pyrite weathering with time in simulated meadow (a) and saline (b) soil solutions.

5. Conclusions

Electrochemistry coupled with surface analysis methods was employed to investigate the pyrite weathering mechanism under simulated meadow and saline soil solutions. The OCP and polarization curves showed that pyrite weathered faster in simulated saline soil or at higher temperatures. Weathering rates were 31.64 and 127.76 g m^{-2} y^{-1} in meadow soil at 5 and 45 °C, respectively; for saline soil, the weathering increased to 60.84 and 141.76 g m^{-2} y^{-1}. EIS results revealed that the causes were the smaller resistance and greater capacitance, and pyrite weathering was related to surface interactions in meadow soil and diffusion-controlled saline soil. CV and surface analysis data showed that pyrite was initially oxidized to $Fe(OH)_3$ and S^0 and released H^+ ions that lowered the pH of the alkaline soil. $Fe(OH)_3$ was further transformed into γ-FeOOH and α-Fe_2O_3, while S^0 was ultimately transformed into sulfate. These results showed that pure pyrite decreased the alkalinity of alkaline soils, while γ-FeOOH and α-Fe_2O_3 effectively reduced the bioavailability of heavy metals with positive effects on bacterial diversity and a lack of toxicity and may find use in future remediation processes. However, heavy metal impurities from impure pyrite scatter into alkaline soils and become potentially problematic pollution sources.

Environmental Implication

Pyrite weathering in alkaline soil would releases H^+ to surrounding circumstances, which may neutralize the soil or turn it acidic and generate acid mine drainage (AMD) if pyrite levels are sufficient. Besides, heavy metal impurities from impurity pyrite scatter into alkaline soils and become potentially problematic pollution sources. In this article, in-situ electrochemical techniques were first used to investigate the weathering behavior of pyrite. To meadow and saline soils environments, the thermodynamics, kinetics and reaction mechanism of pyrite weathering, and amounts of heavy metal ions released in a certain period were obtained. The environmental implications of pyrite weathering were also suggested.

CRediT authorship contribution statement

Bing-Jie Ni: Writing - review & editing. **Qingyou Liu:** Supervision, Writing – review & editing. **Xiaonan Feng:** Methodology, Formal analysis, Data Curation, Writing – original draft. **Zhijie Chen:** Formal analysis, Writing - review & editing. **Shuai Wang:** Formal analysis, Data Curation. **Ling Cen:** Formal analysis, Data Curation.

Declaration of Competing Interest

The authors declare that they have no known competing financial interests or personal relationships that could have appeared to influence the work reported in this paper.

Data Availability

The authors do not have permission to share data.

Acknowledgments

This work was financially supported by the project of the National Natural Science Foundation of China (41873074).

Appendix A. Supporting information

Supplementary data associated with this article can be found in the online version at doi:10.1016/j.jhazmat.2023.131145.

References

[1] Ahlberg, E., 1990. The surface oxidation of pyrite in alkaline solution. J Appl Electrochem 20, 1033–1039.
[2] Badawy, W.A., Al-Kharafi, F.M., Al-Ajmi, J.R., 2000. Electrochemical behaviour of cobalt in aqueous solutions of different pH. J Appl Electrochem 30 (6), 693–704.
[3] Bard, A.J., Faulkner, L.R., 2001. Electrochemical methods: fundamentals and applications, second ed. Wiley, New York.
[4] Cai, Y., Pan, Y., Xue, J., Xue, J., Sun, Q., Su, G., et al., 2009. Comparative XPS study between experimentally and naturally weathered pyrites. Appl Surf Sci 255 (21), 8750–8760.
[5] Caldeira, C.L., Ciminelli, V.S.T., Osseo-Asare, K., 2003. Pyrite oxidation in alkaline solutions: nature of the product layer. Int J Miner Process 72, 373–386.
[6] Chen, Z., Zheng, R., Deng, S., Wei, W., Wei, W., Ni, B.-J., et al., 2021. Modular design of an efficient heterostructured FeS_2/TiO_2 oxygen evolution electrocatalyst via sulfidation of natural ilmenites. J Mater Chem A 9 (44), 25032–25041.
[7] Chen, Z., Zheng, R., Wei, W., Wei, W., B.-J, Chen, H., 2022. Unlocking the electrocatalytic activity of natural chalcopyrite using mechanochemistry. J Energy Chem 68, 275–283.
[8] Corkhill, C.L., Wincott, P.L., Lloyd, J.R., Vaughan, D.J., 2008. The oxidative dissolution of arsenopyrite (FeAsS) and enargite (Cu_3AsS_4) by leptospirillum ferrooxidans. Geochim Cosmochim Acta 72, 5616–5633.
[9] De Donato, P., Kongolo, M., Barres, O., Yvon, J., Enderlé, F., Bouquet, E., et al., 1999. Chemical surface modifications of sulphide minerals after comminution. Powder Technol 105, 141–148.
[10] De Faria, D.L.A., Silva, S.V., De Oliveira, M.T., 1997. Raman microspectroscopy of some iron oxides and oxyhydroxides. J Raman Spectrosc 28, 873–878.
[11] Evangelou, V.P., Huang, X., 1994. Infrared spectroscopic evidence of an iron (II)-carbonate complex on the surface of pyrite. Spectrochim Acta Part A 50, 1333–1340.
[12] Gunawarman G, Refieska A, Ilhamdi I, Affi1 J, Cho K, Nakai M, et al. Corrosion behavior of new beta type Ti-29Nb-13Ta-4.6 zralloy in simulated body fluid solution. In: Proceedings of the conference: frontiers in bioengineering and biotechnology. 10th World Biomaterials Congress; 2016, p. 4.
[13] Hamilton, I.C., Woods, R., 1981. An investigation of surface oxidation of pyrite and pyrrhotite by linear potential sweep voltammetry. J Electroanal Chem 118, 327–343.
[14] Ippolito, J.A., Barbarick, K.A., Elliott, H.A., 2011. Drinking water treatment residuals: a review of recent uses. J Environ Qual 40, 1–12.
[15] Janetski, N.D., Woodburn, S.I., Woods, R., 1977. An electrochemical investigation of pyrite flotation and depression. Int J Miner Process 4, 227–239.
[16] Jang, J.H., Dempsey, B.A., Burgos, W.D., 2007. Solubility of hematite revisited: effects of hydration. Environ Sci Technol 41, 7303–7308.
[17] Joseph, A.R., Kavimandan, S.K., Tilak, K.V., Nain, L., 2014. Response of canola and wheat to amendment of pyrite and sulphur-oxidizing bacteria in soil. Arch Agron Soil Sci 60 (3), 367–375.
[18] Kwon, S.K., Shinoda, K., Shigeru, S., Waseda, Y., 2007. Influence of silicon on local structure and morphology of γ-FeOOH and α-FeOOH particles. Corros Sci 49 (3), 1513–1526.
[19] Laidler, K.J., 1996. A glossary of terms used in chemical kinetics, including reaction dynamics. Pure Appl Chem 68, 149–192.
[20] Lara, R.H., Monroy, M.G., Mallet, M., 2015. An experimental study of iron sulfides weathering under simulated calcareous soil conditions. Environ Earth Sci 73 (4), 1849–1869.
[21] Lasaga, A., 1998. Kinetic theory in the earth sciences. Princeton series in geochemistry. Princeton university press, Princeton, New Jersey.
[22] Lasia, A., 2014. Electrochemical impedance spectroscopy and its applications. Springer, New York, pp. 2–3.
[23] Li, B., Wang, X., Liu, G., Zheng, L., Cheng, C., 2022. Microbial diversity response to geochemical gradient characteristics on AMD from abandoned Dashu pyrite mine in Southwest China. Environ Sci Pollut Res 29, 74983–74997.
[24] Lin, B., Lu, X.Y., Li, L., 2011. Electrochemical corrosion behavior of arc sprayed Zn and $Zn_{15}Al$ coatings in simulated salina soil and neutral meadow soil solutions. J Wuhan Univ Technol Mater Sci Ed 26, 1152–1156.
[25] Liu, Y., Wei, L., Wu, Q., Luo, D., Xiao, T., Wu, Q., et al., 2022. Impact of acid mine drainage on groundwater hydrogeochemistry at a pyrite mine (South China): a study using stable isotopes and multivariate statistical analyses. Environ Geochem Health. https://doi.org/10.1007/s10653-022-01242-8.
[26] Manan, N.S.A., Aldous, L., Alias, Y., Murray, P., Yellowlees, L.J., Lagunas, M.C., et al., 2011. Electrochemistry of sulfur and polysulfides in ionic liquids. J Phys Chem B 115 (47), 13873–13879.
[27] Mohammed, A., Sayed, S., Sherbini, E., Rady, S., 2007. The inhibition of low carbon steel corrosion in hydrochloric acid solutions by succinic acid Part I. weight loss, polarization, EIS, PZC, EDX and SEM studies. Electrochim Acta 52, 3588–3600.
[28] Mycroft, J.R., Bancroft, G.M., McIntyre, N.S., Lorimer, J.W., Hill, I.R., 1990. Detection of sulphur and polysulphides on electrochemically oxidized pyrite surfaces by X-ray photoelectron spectroscopy and Raman spectroscopy. J Electroanal Chem 292 (1), 139–152.
[29] Nesbitt, H., Bancroft, G., Pratt, A., Scaini, M., 1998. Sulfur and iron surface states on fractured pyrite surfaces. Am Mineral 83, 1067–1076.
[30] Nesbitt, H.W., Muir, I.J., Pratt, A.R., 1995. Oxidation of arsenopyrite by air and airsaturated, distilled water and implications for mechanisms of oxidation. Geochim Cosmochim Acta 59, 1773–1786.

[31] Ogbughalua, O.T., Vasileiadis, S., Schumann, R.C., Gerson, A.R., Li, J., Smart, R.S. C., et al., 2020. Role of microbial diversity for sustainable pyrite oxidation control in acid and metalliferous drainage prevention. J Hazard Mater 393, 122338.
[32] Parker, G.K., Woods, R., Hope, G.A., 2008. Raman investigation of chalcopyrite oxidation. Coll Surf A 318, 160–168.
[33] Pinna, M.V., Castaldi, P., Deiana, P., Pusino, A., Garau, G., 2012. Sorption behavior of sulfamethazine on unamended and manure-amended soils and short-term impact on soil microbial community. Ecotoxicol Environ Saf 84, 234–242.
[34] Ramya, S., Krishna, D.N.G., Mudali, U.K., 2018. In-situ Raman and X-ray photoelectron spectroscopic studies on the pitting corrosion of modified 9Cr-1Mo steel in neutral chloride solution. Appl Surf Sci 428, 1106–1118.
[35] Rigby, P.A., Dobos, S.K., Cook, F.J., Goonetilleke, A., 2006. Role of organic matter in framboidal pyrite oxidation. Sci Total Environ 367, 847–854.
[36] Sangaiyal, P., Jayaprakash, R., 2018. A review on iron oxide nanoparticles and their biomedical applications. J Supercond Nov Magn 31, 3397–3413.
[37] Schaufuss, A.G., Nesbitt, H.W., Scaini, M.J., Hoechst, H., Szargan, R., 2000. Reactivity of surface sites on fractured arsenopyrite (FeAsS) toward oxygen. Am Mineral 85 (11–12), 1754–1766.
[38] Shi, Z., Liu, M., Atrens, A., 2010. Measurement of the corrosion rate of magnesium alloys using Tafel extrapolation. Corros Sci 52, 579–588.
[39] Shim, S.H., Duffy, T.S., 2001. Raman spectroscopy of Fe_2O_3 to 62 GPa. Am Miner 87, 318–326.
[40] Tao, D.P., Richardson, P.E., Luttrell, G.H., Yoon, R.H., 2003. Electrochemical studies of pyrite oxidation and reduction using freshly-fractured electrodes and rotating ring-disc electrodes. Electrochim Acta 48, 3615–3623.
[41] Toniazzo, V., Mustin, C., Portal, J.M., Humbert, B., Benoit, R., Err, R., 1999. Elemental sulfur at the pyrite surfaces: speciation and quantification. Appl Surf Sci 143, 229–237.
[42] Tozsin, G., Arol, A.I., Cayci, G., 2015. Use of waste pyrite as an alternative to gypsum for alkaline soil amelioration. Int J Min Reclam Environ 29 (3), 169–177.
[43] Tu, Z.H., Guo, C.L., Zhang, T., Lu, G.N., Wan, J.J., Liao, C.J., et al., 2017. Investigation of intermediate sulfur species during pyrite oxidation in the presence and absence of acidithiobacillus ferrooxidans. Hydrometallurgy 167, 58–65.
[44] Tu, Z.H., Wan, J.J., Guo, C.L., Fan, C., Zhang, T., Lu, G.N., et al., 2017. Electrochemical oxidation of pyrite in pH 2 electrolyte. Electrochim Acta 239, 25–35.
[45] Van der Marel, H.W., Beutelspacher, H., 1976. Atlas of infrared spectroscopy of clay minerals and their admixtures. Elsevier, Amsterdam, p. 396.
[46] Wang, S., Zheng, K., Li, H.P., Feng, X.N., Wang, L.Y., Liu, Q.Y., 2021. Arsenopyrite weathering in acidic water: humic acid affection and arsenic transformation. Water Res 194, 116917.
[47] Wei, W., Feng, X., Chen, Z., Wang, R., Chen, H., 2022. Salt concentration-regulated desalination mechanism evolution in battery deionization for freshwater. ACS Sustain Chem Eng 10 (29), 9295–9302.
[48] Xia, L., Yin, C., Dai, S., Qiu, G., Chen, X., Liu, J., 2010. Bioleaching of chalcopyrite concentrate using leptospirillum ferriphilum, acidithiobacillus ferrooxidans and acidithiobacillus thiooxidans in a continuous bubble column reactor. J Ind Microbiol Biotechnol 37, 289–295.
[49] Zechmeister, H.G., 2013. Bryophytes of continental salt meadows in Austria. J Bryol 27, 297–302.
[50] Zheng, K., Liu, Q., Li, H., 2019. Assessing the influence of humic acids on the weathering of pyrite: electrochemical mechanism and environmental implications. Environ Pollut 51, 738–745.